IEEE Access
Multidisciplinary | Rapid Review | Open Access Journal

Received July 30, 2020, accepted August 6, 2020, date of publication August 11, 2020, date of current version October 12, 2020.

Digital Object Identifier 10.1109/ACCESS.2020.3015850

Research on the Damping Effect Mechanism and Optimization of Super-High-Speed Electric Air Compressors for Fuel Cell Vehicles Under the Stiffness Softening Effect

DONGHAI HU[1], JING WANG[1], LELI HU[1], JIAMING ZHOU[2], AND JIE LIU[3]

[1]School of Automotive and Traffic Engineering, Jiangsu University, Zhenjiang 212013, China
[2]School of Mechanical Engineering, Beijing Institute of Technology, Beijing 100000, China
[3]School of Automotive Engineering, Shandong Jiaotong University, Jinan 250300, China

Corresponding author: Donghai Hu (1000004735@ujs.edu.cn)

This work was supported in part by the National Key Research and Development Program-supported key project "Manufacturing basic technology and key components" under Grant 2018YFB2000704, and in part by the National Natural Science Foundation of China under Grant 51705208.

ABSTRACT As a typical electromechanically coupled system, the super-high-speed permanent magnet synchronous motor (PMSM)-driven compressor always exhibits complex dynamic behavior, affecting the comprehensive performance of the fuel cell system. Based on this, this paper takes electromagnetic and load excitations into account and establishes a mathematical model of the super-high-speed PMSM-driven compressor. Then, the corresponding simulation is carried out, revealing that according to different causes and manifestations, the system gradually exhibits amplitude instability and frequency instability. Considering the stiffness softening effect, the effect of the torsional stiffness and damping coefficient on the dynamic characteristics under different forms of instability is obtained. Using the Routh-Hurwitz criterion and Melnikov theory, a damping optimization methodology is given. The results show that under the condition of amplitude instability, damping reduction and stiffness softening lead to a greater resonant amplitude and a wider resonance region. Under the condition of frequency instability, the system becomes chaotic via periodic-doubling bifurcation with the decrease of damping, and the decrease of torsional stiffness increases the damping required to maintain the stability.

INDEX TERMS Super-high-speed permanent magnet synchronous motor, fuel cell system, stiffness softening, damping Optimization.

I. INTRODUCTION

As a core unit for fuel cell systems, the operation stability of the super-high-speed PMSM-driven compressor influences the comprehensive performance of the fuel cell system significantly, especially the operation efficiency [1], [2]. Generally, a super-high-speed PMSM-driven compressor consists of electric and mechanical domains and is typically considered to be an electromechanically coupled system [3], [4]. Influenced by working conditions and electromechanical coupling effects [5], the super-high-speed PMSM-driven compressor may produce a variety of dynamic behaviors during the operation, reducing the NVH performance and affecting the stability and safety of the super-high-speed PMSM-driven compressor. Therefore, it is important to analyze the instability mechanism during the operation of the super-high-speed PMSM-driven compressor, which has important theoretical significance for the design and operation efficiency optimization of fuel cell systems.

Due to the electromechanical coupling, the super-high-speed motor-driven system will produce complex dynamic phenomena that usually cause serious damage to the mechanical and electrical parts of the system [6]. Numerous scholars have conducted extensive research in this field. Chen [7]–[9] established a torsional vibration model of a powertrain to study the effects of electromechanical parameters on primary resonance characteristics. Bifurcation characteristics of the external excitation amplitude and

The associate editor coordinating the review of this manuscript and approving it for publication was Jinquan Xu.

damping on the system were investigated by applying the Melnikov method. Shi [10], [11] established a mathematical model of the super-high-speed-driven system of a rolling mill by taking internal and external excitations into account. In this study, the multiscale method was used to study the amplitude-frequency response characteristics of the system, and the bifurcation conditions were given. In addition, primary resonance effects due to the damping coefficient and nonlinear stiffness of the system were discussed. Aiming at the problem of the instability phenomenon for a wind turbine drive system, Zhao [12] established a nonlinear dynamic model. The mechanism of vibration evolution of the drive system with changes in parameters, such as the force ratio and time-varying mesh stiffness, was revealed. Liu [13], [14] derived a mathematical model of a super-high-speed relative rotation system taking into consideration the magnetic field energy of an AC motor. The effect of the electromagnetic stiffness on the bifurcation characteristics was studied, and the corresponding conditions of Hopf bifurcation were given. By introducing the Silnikov method, the variation mechanism of system parameters for chaotic motion was studied strictly. Bai [15] proposed a lateral-torsional coupled dynamics model of a super-high-speed motor-driven system, and it was found that additional and severe gear vibrations would be induced under the effect of electromechanical coupling. For super-high-speed motors, long-term super-high-speed operation may cause the shafting stiffness to soften, causing additional instability phenomena. In this event, the dynamic response will be more complicated, and the operation efficiency will be further affected. However, the previous studies neglected the influence of the stiffness softening effect when analyzing the instability behavior of the super-high-speed motor-driven system, and the research object was mainly an induction motor or electrical excitation-based hydroelectric generators. Therefore, investigating the instability mechanism and optimizing the design parameters under the stiffness softening effect are of theoretical and practical significance for super-high-speed PMSM-driven systems.

The rest of this article is structured as follows. Taking electromagnetic and load excitations into consideration, a nonlinear dynamic model of a compressor powered by a super-high-speed PMSM is established in Section 2. The dynamic characteristics and the instability types of the system are revealed and defined under different excitation frequencies by carrying out detailed simulations in Section 3. In Section 4, the multiscale method is employed to derive the amplitude-frequency response characteristic under the condition of amplitude instability. Considering the stiffness softening effect of the super-high-speed PMSM-driven compressor, the effect of torsional stiffness and damping on the dynamic behavior is studied through numerical simulations. Moreover, damping optimization methods are also given. In Section 5, the dynamic characteristics of the super-high-speed PMSM-driven compressor under frequency instability are analyzed. The influencing factors are studied, and a damping optimization method is given. Section 6 compares

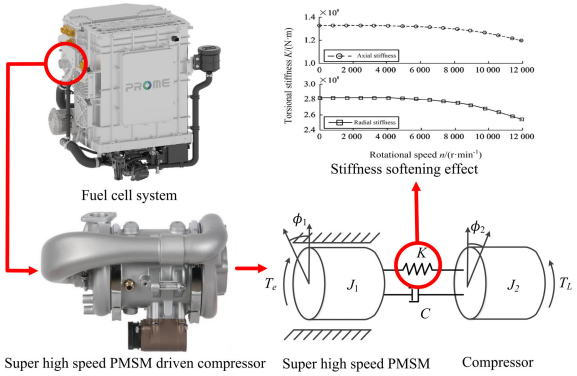

FIGURE 1. Two-mass model of the super-high-speed PMSM-driven compressor.

results of our approach and others regarding the dynamic characteristics of the super-high-speed motor-driven system. In Section 7, the final remarks of this paper are presented. Additionally, the contributions of this work are given below:

1. This paper establishes a dynamic model of a compressor powered by a super-high-speed PMSM, and the instability type of the system is determined according to the different causes and manifestations.

2. Considering the stiffness softening effect, the effects of torsional stiffness and damping on the destabilizing behavior of the super-high-speed PMSM-driven compressor are discussed.

3. As an important factor in the super-high-speed PMSM-driven compressor, the damping in different instability conditions is optimized by applying the Routh-Hurwitz criterion and Melnikov method in this paper.

II. MATHEMATICAL MODEL OF A COMPRESSOR POWERED BY A SUPER-HIGH-SPEED PMSM

The compressor powered by the super-high-speed PMSM of a fuel cell system is selected as the research object in this paper, and Figure 1 illustrates that the system obviously can be equivalent to a two-mass model based on the operation principle. Moreover, under the action of the centrifugal force and gyroscopic moment of the rolling element, it can be found that the stiffness of the drive shaft decreases with increasing rotational speed.

In this section, we use the generalized Lagrange equation to establish the dynamic equation of the super-high-speed PMSM-driven compressor.The total kinetic energy of the system is

$$T = \sum_{i=1}^{2} \frac{1}{2} J_i \dot{\phi}_i^2 = \frac{1}{2} J_i \dot{\phi}_1^2 + \frac{1}{2} J_i \dot{\phi}_2^2 \tag{1}$$

The potential energy of the system is

$$V = \frac{1}{2} K(\phi_1 - \phi_2)^2 \tag{2}$$

where ϕ_1 and ϕ_2 are the rotation angles. $\dot{\phi}_1$ and $\dot{\phi}_2$ are the rotational speed of the motor rotor and load, respectively.

J_1 and J_2 are the rotor inertia and the load inertia, respectively. K is the torsional stiffness.

Taking the magnetic field energy of the super-high-speed PMSM into consideration, the Lagrangian function L and dissipation function F are given by

$$L = T - V = \frac{1}{2}J_i\dot{\phi}_1^2 + \frac{1}{2}J_i\dot{\phi}_2^2 - \frac{1}{2}K(\phi_1 - \phi_2)^2 \quad (3)$$

$$F = \frac{1}{2}C(\dot{\phi}_1 - \dot{\phi}_2)^2 + \frac{1}{2}C_e\dot{\phi}_1^2 \quad (4)$$

where C and C_e are the shaft damping coefficient and the electromagnetic damping coefficient, respectively. The magnetic energy in the air-gap field of the super-high-speed PMSM is

$$W = \frac{Rl_e}{2}\int_0^{2p\pi} \Lambda F^2(\alpha, t)d\alpha \quad (5)$$

where R and l_e are the inner radius and the effective length of the rotor, respectively, Λ is the air-gap magnetic conductivity of the PMSM, and $\Lambda = \frac{\mu_0}{k_\mu \delta_0}$. μ_0 and k_μ are the air magnetic permeability and magnetic saturation coefficient, respectively. The fundamental synthetic magnetomotive force (MMF) of the super-high-speed PMSM is

$$\begin{aligned} F(\alpha, t) &= F_{sm}\cos(\omega t - \alpha) \\ &\quad + F_{rm}\cos\left[\omega t - \alpha + (p\varphi_1 + \psi + \frac{\pi}{2})\right] \end{aligned} \quad (6)$$

where F_{sm} and F_{rm} are the amplitude of the MMF of the stator and rotor, respectively, which are shown below.

$$\begin{aligned} F_s(\alpha, t) &= F_{sm}\cos(\omega t - \alpha) \\ &= 1.35\frac{NI_r k_N}{p}\cos(\omega t - \alpha) \end{aligned} \quad (7)$$

$$\begin{aligned} F_r(\alpha, t) &= F_{rm}\cos(\omega t - \alpha) \\ &= \frac{4B_r h_m}{\pi\mu_0}\sin(\frac{\alpha_p\pi}{2})\cos(\omega t - \alpha) \end{aligned} \quad (8)$$

where p represents the pole pairs; N is the number of series windings of each phase; I_r is the rated current; h_m, B_r and α_p are the thickness, magnetic remanence and pole arc coefficient, respectively; and k_N and ω are the winding coefficient and the electric angular frequency, respectively. The electromagnetic torque can be obtained as

$$T_e = \frac{dW}{d(p\varphi_1)} \quad (9)$$

Substituting Eqs.(5) - (8) into Eq.(9), the electromagnetic torque expression of the super-high-speed PMSM can be derived as follows:

$$T_e = k_0 + k_1\varphi_1 - k_1\varphi_1^2 - k_3\varphi_1^3 \quad (10)$$

where $F_m = p\pi Rl\Lambda_0 F_{sm}F_{rm}$, $k_0 = F_m\cos\psi$, $k_1 = pF_m\sin\psi$, $k_2 = p^2k_0/2$, and $k_3 = p^2k_1/6$.

Introducing the dissipation Lagrange equation

$$\frac{d}{dt}\left(\frac{\partial L}{\partial\dot{q}_i}\right) - \frac{\partial L}{\partial q_i} + \frac{\partial F}{\partial\dot{q}_i} = Q_i(i = 1, 2) \quad (11)$$

and substituting the Lagrangian function Eq.3 into Eq.11, the dynamic equations of the super-high-speed PMSM-driven compressor are expressed as

$$\begin{cases} J_1\ddot{\phi}_1 + C(\dot{\phi}_1 - \dot{\phi}_2) + K(\phi_1 - \phi_2) = T_e \\ J_2\ddot{\phi}_2 - C(\dot{\phi}_1 - \dot{\phi}_2) - K(\phi_1 - \phi_2) = -T_L \end{cases} \quad (12)$$

where T_e and T_L are the electromagnetic torque and load torque, respectively. Considering the load excitation, we can obtain

$$\begin{cases} T_e = T_{e0} + \Delta T_e \\ T_L = T_{L0} + \Delta T_L \end{cases} \quad (13)$$

where T_{e0} and T_{L0} are the constant parts of the torque. ΔT_e and ΔT_L are the disturbance parts.

In this work, ϕ_{10} and ϕ_{20} are the torsional angles of the motor end and load end, respectively, and φ_1 and φ_2 are the torsional vibration angles caused by the disturbance torque of the motor and load. Then, the relationship between the rotation angles can be obtained as

$$\begin{cases} \phi_1 = \phi_{10} + \varphi_1, \phi_2 = \phi_{20} + \varphi_2 \\ \dot{\phi}_{10} = \dot{\phi}_{20}, \ddot{\phi}_{10} = \ddot{\phi}_{20} = 0 \end{cases} \quad (14)$$

The following dynamic equation can be obtained:

$$\begin{cases} J_1\ddot{\varphi}_1 + C(\dot{\varphi}_1 - \dot{\varphi}_2) + K(\varphi_1 - \varphi_2) = \Delta T_e \\ J_2\ddot{\varphi}_2 - C(\dot{\varphi}_1 - \dot{\varphi}_2) - K(\varphi_1 - \varphi_2)) = -\Delta T_L \end{cases} \quad (15)$$

According to reference [8], it can be assumed that the disturbance part of the load torque is in the form of $\Delta T_L = F\cos(\omega t)$. According to Eq.(10), we can obtain the electromagnetic disturbance $\Delta T_e = k_1\varphi_1 - k_1\varphi_1^2 - k_3\varphi_1^3$. Let $x = \phi_1 - \phi_2$, and substitute these into Eq.(5). The dimensionless form of the nonlinear dynamic equation for the compressor powered by the super-high-speed PMSM can be obtained:

$$\ddot{x} + \eta^2 x + \mu\dot{x} + \beta x^2 + \gamma x^3 = f\cos\omega t \quad (16)$$

where

$$\eta^2 = \omega_0^2 - \kappa, \quad \mu = \left(\frac{1}{J_1} + \frac{1}{J_2}\right)C$$

$$\kappa = \frac{k_1 r}{J_1}, \quad \beta = \frac{k_r^2}{J_1}, \ \gamma = \frac{k_3 r^3}{J_1}, \ \nu = \frac{J_1}{J_2}$$

$$f = \frac{F}{J_2}, \quad r = \frac{1}{1+\nu}, \ \omega_0 = \sqrt{\left(\frac{1}{J_1} + \frac{1}{J_2}\right)K}$$

III. DETERMINATION OF THE MOTION STATE

Serious problems associated with the complex dynamic behavior in super-high-speed PMSM-driven compressors are obvious under load and electromagnetic excitations. To explore the dynamic behavior expressions of the super-high-speed PMSM-driven compressor under different conditions, numerical simulations are carried out.

According to super-high-speed PMSM-driven compressor parameters and related equations, we can obtain $\eta = 3$, $\beta = 9$, and $\gamma = 3$. We take $x = 0$, and $y = 0$ as the initial

TABLE 1. Main parameters used in this research.

Parameter	Value	Unit
Rated power, P_0	30	kW
Rated speed, ω_0	60000	rpm
Pole pairs, p	4	
Each phase series windings, N	110	
Inner radius of rotor, R	55	mm
Magnet thickness, h_m	8	mm
Length of stator core, l	85	mm
Length of air gap, δ_0	1.5	mm
Inertia of machine rotor, J_1	0.081	kg·m^2
Inertia of load rotor, J_2	0.21	kg·m^2

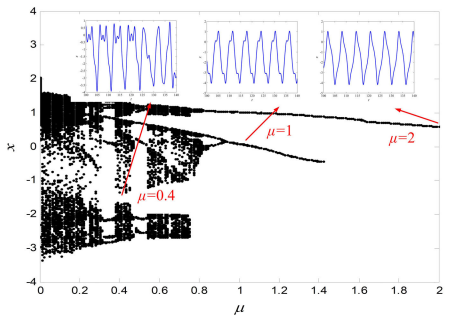

(a)

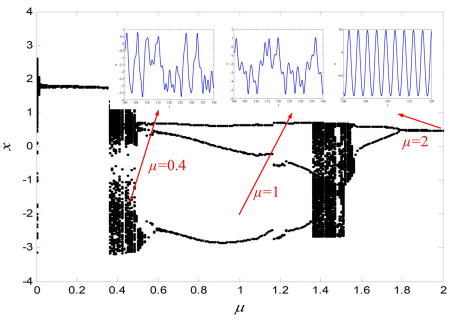

(b)

FIGURE 2. Bifurcation diagrams using μ as the control parameter: (a) $\omega = 1$; (b) $\omega = 3$.

conditions and the excitation frequency $\omega = 1$ and $\omega = 3$ separately. Damping values of $\mu = 0.4$, 1, and 2, are taken and the corresponding time histories are attached to the corresponding bifurcation diagram, which is shown in Figure 2. It can be found in Figure 2(a) that when the damping is 0.4, the time history shows disordered vibration, and the system is chaotic. The system exhibits an irregular movement, and the oscillation frequency changes and loses stability with the amplitude unchanged over time, which indicates that the system becomes chaotic. In this case, Figure 2(b) exhibits totally different characteristics compared to Figure 2(a). The oscillation amplitude of the system jumps at this time, and the system loses stability and generates resonance. When the damping is 1, Figure 2(a) illustrates that the system is in quasi-periodic motion and gradually becomes stable. However, Figure 2(b) shows that the oscillation amplitude varies continuously with the frequency unchanged, and the system is still in a resonant state. As the damping further increases, when the damping is 2, it is easy to find from the corresponding time history diagram that the system instability is suppressed at this time, and the system exhibits a stable periodic motion. From this finding, we can conclude that in addition to stable motion, we can define the motion state of the system as resonance and chaos according to the difference in the amplitude and frequency instability.

IV. DAMPING OPTIMIZATION BASED ON AMPLITUDE INSTABILITY

A. DYNAMIC CHARACTERISTICS ANALYSIS

To analyze the evolution of the dynamics of the system when the amplitude exhibits instability, we introduced a multiscale method to solve equation Eq.(16). The first-mode approximation is considered in this paper, and it is employed to derive the response equation of the system. The damping term and the electromagnetic parameter term are restricted by ε. The external excitation frequency ω is expressed as

$$\omega = \omega_0 + \varepsilon\sigma \tag{17}$$

where σ, the frequency offset parameter, is used to indicate the proximity of the external excitation frequency ω and the inherent frequency ω_0. Therefore, to study the primary resonance, Eq.(16) must be rearranged as follows:

$$\ddot{x} + \omega_0^2 x = -\varepsilon(\mu\dot{x} + \beta x^2 + \gamma x^3) + \varepsilon f \cos\omega t \tag{18}$$

Based on the conventional multiscale method, the form of the solution is assumed as

$$x(t) = x_0(T_0, T_1) + \varepsilon x_1(T_0, T_1) \tag{19}$$

where $T_r = \varepsilon^r t$. By defining $D_r = d/dT_r$, the derivative operator can be expressed as

$$\begin{aligned}\frac{d}{dt} &= \sum_{r=0}^{+\infty} \varepsilon^r D_r = D_+ \varepsilon D_+ \varepsilon^2 D_2 + \cdots \\ \frac{d^2}{dt^2} &= \sum_{r=0}^{+\infty} \varepsilon^r D_r (\sum_{s=0}^{+\infty} \varepsilon^s D_s) \\ &= D_0^2 + 2\varepsilon D_0 D_1 + \varepsilon^2 (d_1^2 + 2D_0 D_2) + \cdots\end{aligned} \tag{20}$$

Substituting Eq.(19) into Eq.(18), the following partial differential equations can be obtained:

$$\begin{aligned}\varepsilon^0 &: D_0^2 x_0 + \omega_0^2 x_0 = 0 \\ \varepsilon^1 &: D_0^2 x_1 + \omega_0^2 x_1 = -2D_0 D_1 x_0 - \mu D_0 x_0 - \beta x_0^2 \\ &\qquad - \gamma x_0^3 + f\cos(\omega_0 T_0 + \sigma T_1)\end{aligned} \tag{21}$$

Then, the general solution associated with ε^0 in Eq.(21) can be expressed as

$$x(t) = a(T_1)\cos[\omega_0 T_0 + \beta(T_1)] = A(T_1)e^{j\omega_0 T_0} + cc \tag{22}$$

where cc denotes the conjugate of the preceding term. A can be defined in polar form as

$$A(T_1) = \frac{1}{2}a(T_1)e^{j\zeta(T_1)} \tag{23}$$

where α and ζ are both functions of T_1.

Substituting Eq.(22) into the second equation in Eq.(21), the following equation is obtained:

$$\begin{aligned} D_0^2 x_1 + \omega_0^2 x_1 = & -j\omega_0(2D_1A + \mu A)e^{j\omega_0 T_0} \\ & - \beta(A^2 e^{2j\omega_0 T_0} + A\bar{A}) \\ & - \gamma(A^3 e^{3} j\omega_1 T_0 + 3A^2\bar{A}e^{j\omega_0 T_0}) \\ & + \frac{1}{2} f e^{j(\omega_0 T_0 + \sigma T_1)} + cc \end{aligned} \tag{24}$$

Eliminating secular terms, we can obtain

$$j\omega_0(2D_1A + \mu A) + 3\gamma A^2\bar{A} - \frac{1}{2} f e^{j\sigma T_1} = 0 \tag{25}$$

Introducing $\varphi = \sigma T_1 - \zeta$, the imaginary and real parts can be respectively expressed as

$$\begin{cases} D_1 a = -\dfrac{1}{2}\mu a + \dfrac{f}{2\omega_0}\sin\varphi \\ a D_1\varphi = \sigma a - \dfrac{3\gamma}{8\omega_0}a^3 + \dfrac{f}{2\omega_0}\cos\varphi \end{cases} \tag{26}$$

The energy is conserved at the equilibrium point. The amplitude and phase remain unchanged, and the relative system exhibits steady motion. Due to this, steady-state responses occur when $D_1 a = D_1\varphi = 0$. The amplitude-frequency response equation of the system can be correspondingly obtained,

$$\left[\left(\frac{1}{2}\varepsilon\mu\right)^2 + \left(\omega - \omega_0 - \frac{3\varepsilon\gamma}{8\omega_0}a^2\right)^2\right] a^2 = \left(\frac{\varepsilon f}{2\omega_0}\right)^2 \tag{27}$$

Solving Eq.(27), the expression of the excitation frequency ω associated with amplitude a can be obtained,

$$\omega = \omega_0 + \frac{3\varepsilon\gamma}{8\omega_0}a^2 \pm \sqrt{\left(\frac{\varepsilon f}{2\omega_0 a}\right)^2 - \left(\frac{\varepsilon\mu}{2}\right)^2} \tag{28}$$

The amplitude-frequency response curve of the primary resonance can be obtained by Eq.(28), which is shown in Figure 3. It can be found that the number of the solution changes with ω. The stability of solutions is marked in Figure 3, in which the solid line and dotted line represent the stable set and unstable set, respectively. Additionally, as the excitation frequency ω changes, a jumping phenomenon is generated, affected by the unstable solutions. The trajectory moves along the curve ABC with increasing ω until the amplitude a reaches its maximum value. The jump phenomenon occurs with the further increase in ω at point C, and the amplitude jumps from point C to point D. At this time, the trajectory moves along the curve DEF with decreasing ω until it reaches the critical saddle point F. The jump phenomenon is generated again with a further decrease in ω. The generation of the saddle node bifurcation and jump phenomenon makes it easier to cause fatigue damage to drive the shaft, affecting the stable operation of the system.

After analysis, the maximum amplitude of the primary resonance of the super-high-speed PMSM-driven compressor can be expressed as

$$a_{max} = \frac{f}{\omega_0\mu} \tag{29}$$

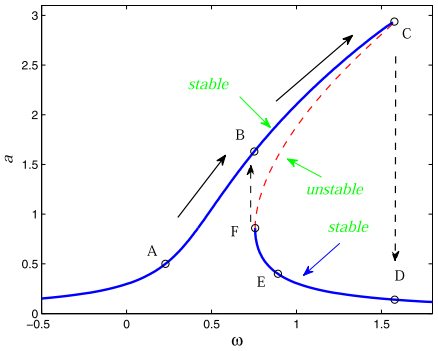

FIGURE 3. Amplitude-frequency response characteristics.

The excitation frequency ω at which the maximum amplitude occurs can be correspondingly obtained,

$$\omega = \omega_0 + \frac{3\varepsilon\gamma}{8\omega_0}a_{max}^2 \tag{30}$$

Generally, the curve determined by Eq.(30) is called the skeleton line of primary resonance, which dominates the shape of the amplitude-frequency response curve for primary resonance. It can be found that the maximum amplitude a_{max} and the corresponding frequency ω are related to the damping μ.

$\mu = 1, 3,$ or 5 is taken to analyze the effect of damping on the amplitude-frequency response. Figure 4 presents the response curves with different dampings when the torsional stiffness $K = 2 \times 10^5$. It can be seen that the damping will affect the amplitude of the system and the bending degree of the curve. The skeleton line shifts to the left and the amplitude decreases with enlargement of damping μ. The displacement of the skeleton line makes the resonance area of the system decrease (as the dashed line in Figure 4(a) shows), implying that the stable operation range of the system increases as the damping enlarges. When $\mu = 2$, the left shift range has reached almost 90 percent, greatly increasing the stable operating boundary and reducing the resonance possibility. Therefore, the damping change of the transmission system should be controlled within a reasonable range, which is conducive to the stable operation of the transmission system.

However, in the case of high speed operation, the torsional stiffness of the drive shaft may rapidly decrease as the motor speed is raised. The corresponding amplitude-frequency responses are shown in Figures 4(b) - 4(d). It can be obviously found that in the case of the same damping, the skeleton line bends to the right as the torsional stiffness decreases. For instance, when $\mu = 5$, as the torsional stiffness K drops from 2×10^5 to 1×10^5, the resonance area covered by the skeleton line almost increases by 5 times, which greatly increases the instability probability of the system. In addition, it can also be found that the amplitude of the primary resonance increases with the change in stiffness. This phenomenon shows that for super-high-speed transmission systems, the stiffness softening likely induces a transition into the resonance state during the operation. Therefore, it is necessary to design the damping

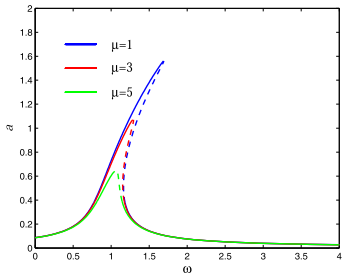

(a)

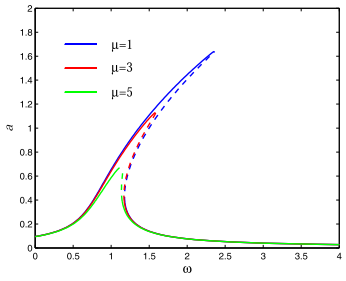

(b)

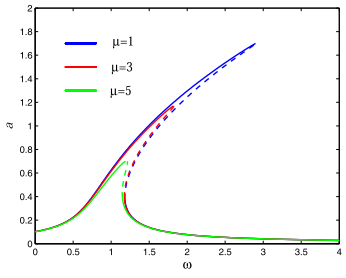

(c)

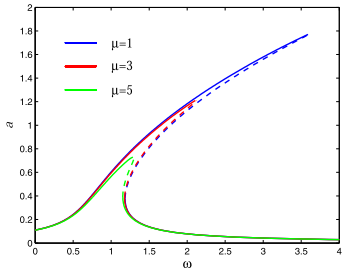

(d)

FIGURE 4. Amplitude-frequency response characteristics for $K = 2 \times 10^5$, 1.5×10^5, 1.2×10^5, and 1×10^5.

based on the stiffness corresponding to the maximum speed so that stable operation can be guaranteed.

B. DAMPING OPTIMIZATION METHODOLOGY

According to the above analysis, under the condition of amplitude instability, changes in the damping and stiffness may have a significant impact on the dynamic characteristics. Therefore, it is essential to optimize the damping in the design stage.

Here, we rewrite Eq.(26). Linearizing Eq.(26) at (a, φ), an autonomous differential equation involving Δa and $\Delta\varphi$ is formed,

$$\begin{cases} D_1 \Delta a = -\dfrac{1}{2}\mu \Delta a + \dfrac{f}{2\omega_0}\cos\varphi \Delta\varphi \\ aD_1 \Delta\varphi = \sigma \Delta a - \dfrac{9\gamma}{8\omega_0}a^2 \Delta a - \dfrac{f}{2\omega_0}\sin\varphi \Delta\varphi \end{cases} \tag{31}$$

Based on the Routh-Hurwitz criterion, the following eigenvalue equation can be obtained:

$$\begin{vmatrix} -\dfrac{1}{2}\mu - \lambda & -a\left(\sigma - \dfrac{3\gamma}{8\omega_0}a^2\right) \\ \dfrac{1}{a}\left(\sigma - \dfrac{9\gamma}{8\omega_0}a^2\right) & -\dfrac{1}{2}\mu - \lambda \end{vmatrix} = 0 \tag{32}$$

where λ represents the eigenvalues of the Jacobian matrix. Expanding this determinant,

$$\lambda^2 + \mu\lambda + \frac{1}{4}\mu^2 + \left(\sigma - \frac{3\gamma}{8\omega_0}a^2\right)\left(\sigma - \frac{9\gamma}{8\omega_0}a^2\right) = 0 \tag{33}$$

According to the Routh-Hurwitz criterion, we can obtain the damping range that keeps the system stable:

$$\mu > 2\sqrt{-\left(\sigma - \frac{3\gamma}{8\omega_0}a^2\right)\left(\sigma - \frac{9\gamma}{8\omega_0}a^2\right)} \tag{34}$$

V. DAMPING OPTIMIZATION BASED ON FREQUENCY INSTABILITY

A. DYNAMIC CHARACTERISTICS ANALYSIS

Before studying the dynamic characteristics under frequency instability, the excitation term and damping term of the system are regarded as small perturbations, and Eq.(16) is rewritten. The rewritten dynamic equation is as follows:

$$\begin{cases} \dot{x} = y \\ \dot{y} = -\omega_0^2 x - \beta x^2 - \gamma x^3 - \mu_1 x + f_1 \cos\omega t \end{cases} \tag{35}$$

where $\mu_1 = \varepsilon\mu, f_1 = \varepsilon f$. ε is a small parameter, and generally, $\varepsilon \ll 1$.

Detailed simulations have been performed to analyze the instability behavior concerning damping and to obtain the chaotic behavior for Eq.(35). In addition, the default of the torsional stiffness is $K = 2 \times 10^5$ at this time. Taking $\mu_1(\mu_1 = \varepsilon\mu)$ as a bifurcation parameter, the bifurcation diagram of the super-high-speed PMSM-driven compressor is presented in Figure 5. The findings indicate that the super-high-speed PMSM-driven compressor generates very rich nonlinear phenomena with the change in μ_1. It can be found that the super-high-speed PMSM-driven compressor exhibits a 1T-periodic response when $\mu_1 > 0.9$. However, as μ_1 drops to 0.4, a quasi-periodic motion replaces the 1T-periodic motion. With a further decrease of the control parameter μ_1, chaotic motion is generated in the system after period-doubling bifurcations. Finally, periodic and chaotic motion occur alternately.

To provide a clearer illustration, three values ($\mu_1 = 0.2$, $\mu_1 = 0.4$ and $\mu_1 = 0.9$) are chosen to carry out numerical

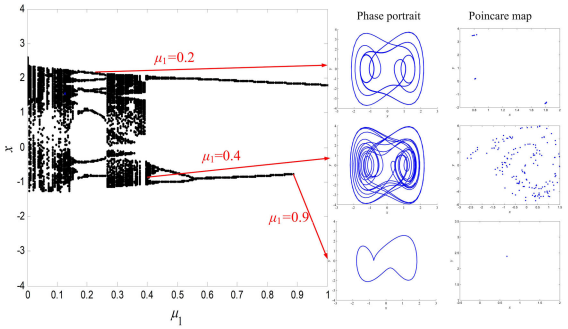

FIGURE 5. Bifurcation characteristics when $K = 2 \times 10^5$.

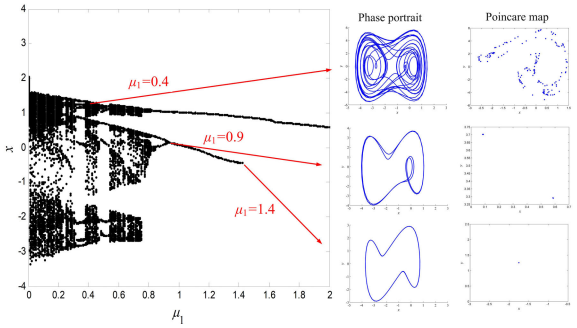

FIGURE 6. Bifurcation characteristics when $K = 1.5 \times 10^5$.

simulations to show the transformation of chaos. The corresponding phase portrait and Poincare map are attached to the bifurcation diagram. According to Figure 5, $\mu_1 = 0.9$ is related to the 1T-periodic motion. The simulations are developed for this value, and the results validate the above analysis. As μ_1 decreases and crosses the critical value ($\mu_1 = 0.9$), the system gradually exhibits chaotic behavior. Simulations are performed on the parameters related to $\mu_1 = 0.4$. From the phase portrait and Poincare map, chaotic behavior is clearly visible. As mentioned above, with μ_1 further decreasing, periodic and chaotic motion occur alternately. Numerical analysis is performed on the parameters related to $\mu_1 = 0.2$. The phase portrait and Poincare map corresponding to the quasi-periodic motion are presented.

However, considering the stiffness softening effect existing in the transmission system during high-speed operation, we take torsional stiffness $K = 1.5 \times 10^5$ and 1.2×10^5. Figure 6 and Figure 7, respectively, show the bifurcation characteristics under these conditions. Comparing these bifurcation diagrams, it is obvious that although the overall trend of the change is similar, the damping required to maintain the stability of the system increases significantly with decreasing stiffness. When torsional stiffness $K = 2 \times 10^5$, the critical value of damping is 0.9. However, when the torsional stiffness drops to 1.5×10^5 and 1.2×10^5, the critical value correspondingly changes to 1.4 and 1.7. A series of numerical simulations are performed to verify the analysis. For Figure 6, three values ($\mu_1 = 0.4$, $\mu_1 = 0.9$ and $\mu_1 = 1.4$) are

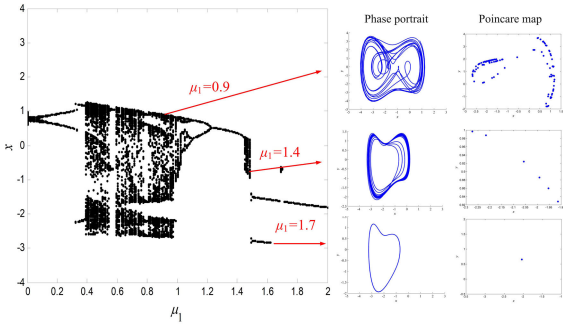

FIGURE 7. Bifurcation characteristics when $K = 1.2 \times 10^5$.

chosen, and the phase portrait and Poincare map are attached to Figure 6. It can be seen that for $\mu_1 = 0.4$, the system exhibits chaotic motion, similar to that of Figure 5. In terms of $\mu_1 = 0.9$, this is the critical value for Figure 5, and the system is in a stable state. However, with the torsional stiffness decreasing to $K = 1.5 \times 10^5$, the 2T-periodic motion replaces the 1T-periodic motion, and the system begins to lose stability. According to the phase portrait and Poincare map, it is easy to find that in this case, the system enters a stable state only when the damping μ_1 reaches the critical value 1.4. As the torsional stiffness further decreases to $K = 1.2 \times 10^5$, numerical simulations are performed on the parameters related to $\mu_1 = 0.9$, $\mu_1 = 1.4$ and $\mu_1 = 1.4$. As mentioned above, $\mu_1 = 0.9$ and $\mu_1 = 1.4$ are the critical values of the damping for the system in the case of $K = 2 \times 10^5$ and $K = 1.5 \times 10^5$, respectively. From the corresponding phase portraits and Poincare maps in Figure 7, it can be seen that under these two sets of values, the system is in a state of instability. Furthermore, the system enters a stable state only when the damping μ_1 reaches the critical value of 1.7, which confirms the above analysis.

B. DAMPING OPTIMIZATION METHODOLOGY

In this section, the Melnikov method is employed to calculate the critical value of damping and analyze the homoclinic bifurcation of the model. The transformed vector form of Eq.(35) is

$$\begin{cases} \dot{x} = p_1(x, y) + \varepsilon q_1(x, y, \tau) \\ \dot{y} = p_2(x, y) + \varepsilon q_2(x, y, \tau) \end{cases} \tag{36}$$

where $p_1(x, y) = y$, $q_1(x, y, \tau) = 0$, $p_2(x, y) = -\omega_0^2 x - \beta x^2 - \gamma x^3$, and $q_2(x, y, \tau) = -\mu_1 x + f_1 \cos \omega t$.

According to the Melnikov theorem, the Melnikov equation can be written as

$$M(\tau_0) = \int_{-\infty}^{+\infty} p(X_h(\tau)) \wedge q(X_h(\tau), \tau + \tau_0) d\tau \tag{37}$$

where $X_h(\tau) = (x_h, y_h)$ represents homoclinic orbits, and $p \wedge q = p_1 q_2 - p_2 q_1$. τ_0 is the the initial time of the forcing term. The Melnikov integral can be expressed as follows by

substituting Eq.(36) into Eq.(37):

$$M(\tau_0) = \int_{-\infty}^{+\infty} [-\mu_1 y_h(\tau + f_1 cos\omega(\tau + \tau_0))]\, y_h(\tau) d\tau = -\mu_1 I_1 + f_1 I_2 sin\omega\tau_0 \quad (38)$$

where the component integrals I_1 and I_2 are

$$I_1 = \int_{-\infty}^{+\infty} y_h(\tau) d\tau$$

$$I_2 = -\int_{-\infty}^{+\infty} y_h sin(\omega\tau) d\tau$$

The conditions for the cross-section of the stable and unstable manifold are $M(\tau_0) = 0$ and $dM(\tau_0)/d\tau_0 \neq 0$. Therefore, the threshold for parameter stability can be obtained,

$$\mu > f \left| \frac{I_2}{I_1} \right| \quad (39)$$

VI. DISCUSSION

For the super-high-speed PMSM-driven compressor, a long-time duration in the high-speed state may induce shaft stiffness softening, and complex dynamic phenomena will be generated that cause substantial damage to the transmission components, affecting the operational stability of the super-high-speed PMSM-driven compressor. Based on the stiffness softening effect, the instability mechanism and an optimization design methodology are investigated in this paper. It can be found that the system mainly manifests resonance and chaos according to the different factors and manifestations. The specific forms of instability can be divided into amplitude instability and frequency instability. When the amplitude loses stability, an increase in damping decreases the resonant region and resonant amplitude. Moreover, stiffness softening makes the system more likely to resonate. In addition, by analyzing the frequency instability of the system, it can be found that a reduction in damping may result in the system becoming chaotic through periodic-doubling bifurcation. The stiffness softening effect would increase the damping required to maintain the stability of the system.

In previous studies, although references [8], [12]–[18] have studied the dynamic behaviors of the super-high-speed motor-driven system, the research object was mainly an induction motor or electrical excitation-based hydroelectric generators. Moreover, they generally ignored the stiffness softening effect and its impact on system design and dynamic analysis. The research in this paper shows that the stiffness softening effect is crucial for the dynamic analysis of super-high-speed motor drive systems, and it also has theoretical guiding significance for the system design.

VII. CONCLUSION

A mathematical model of a super-high-speed PMSM-driven compressor for a fuel cell system under multiple excitations is established in this paper, and the influence factors of the dynamic characteristics are investigated by taking the stiffness softening effect into consideration. The following results are obtained:

1. According to the different causes and manifestations, the system gradually exhibits amplitude instability and frequency instability with changes in the excitation frequency and parameters.

2. Through the study of the amplitude instability, it can be found that changes in the damping and torsional stiffness will lead to an amplitude jump phenomenon. Moreover, smaller damping and stiffness may lead to a greater resonant amplitude, a wider resonance region, and a larger unstable region.

3. Through the study of frequency instability, it is found that with decreasing damping, the system becomes chaotic via periodic-doubling bifurcation. In addition, due to the stiffness softening, a decrease in the torsional stiffness would increase the damping required to maintain stability.

4. Considering the effect of stiffness softening, the Routh-Hurwitz criterion and the Melnikov method are introduced to optimize the damping to ensure operational stability of the super-high-speed PMSM-driven compressor for the fuel cell system.

The results of this paper provide a theoretical reference for future research work regarding the design and operation optimization of the super-high-speed PMSM-driven compressor for fuel cell systems.

REFERENCES

[1] H.-J. Chiu and L.-W. Lin, "A bidirectional DC–DC converter for fuel cell electric vehicle driving system," *IEEE Trans. Power Electron.*, vol. 21, no. 4, pp. 950–958, Jul. 2006.

[2] K. M. Rahman, N. R. Patel, T. G. Ward, J. M. Nagashima, F. Caricchi, and F. Crescimbini, "Application of direct-drive wheel motor for fuel cell electric and hybrid electric vehicle propulsion system," *IEEE Trans. Ind. Appl.*, vol. 42, no. 5, pp. 1185–1192, Sep. 2006.

[3] K. Liu and Z. Q. Zhu, "Online estimation of the rotor flux linkage and voltage-source inverter nonlinearity in permanent magnet synchronous machine drives," *IEEE Trans. Power Electron.*, vol. 29, no. 1, pp. 418–427, Jan. 2014.

[4] Q. Wei and X.-Y. Wang, "Chaos controlling of permanent magnet synchronous motor base on dither signal," *J. Vib. Control*, vol. 19, no. 16, pp. 2541–2550, Dec. 2013.

[5] R. Shanmugasundram, K. M. Zakaraiah, and N. Yadaiah, "Effect of parameter variations on the performance of direct current (DC) servomotor drives," *J. Vib. Control*, vol. 19, no. 10, pp. 1575–1586, Jul. 2013.

[6] L. Wu, S. Yang, Y. Bai, and J. M. Machado, "Efficient robust optimization based on polynomial chaos and tabu search algorithm," *Int. J. Appl. Electromagn. Mech.*, vol. 39, nos. 1–4, pp. 145–150, Sep. 2012.

[7] X. Chen, S. Yuan, and Z. Peng, "Nonlinear vibration for PMSM used in HEV considering mechanical and magnetic coupling effects," *Nonlinear Dyn.*, vol. 80, nos. 1–2, pp. 541–552, Apr. 2015.

[8] X. Chen, J. Hu, Z. Peng, and C. Yuan, "Bifurcation and chaos analysis of torsional vibration in a PMSM-based driven system considering electromechanically coupled effect," *Nonlinear Dyn.*, vol. 88, no. 1, pp. 277–292, Apr. 2017.

[9] X. Chen, H. Wei, T. Deng, Z. He, and S. Zhao, "Investigation of electromechanical coupling torsional vibration and stability in a high-speed permanent magnet synchronous motor driven system," *Appl. Math. Model.*, vol. 64, pp. 235–248, Dec. 2018.

[10] P. Shi, J. Li, J. Jiang, B. Liu, and D. Han, "Nonlinear dynamics of torsional vibration for rolling mill's main drive system under parametric excitation," *J. Iron Steel Res. Int.*, vol. 20, no. 1, pp. 7–12, 2013.

[11] P. Shi, K. Xia, B. Liu, and D. Hou, "Non-main resonance characteristics of nonlinear torsional vibration of rolling mill's multi-degree-of-freedom main drive system," *J. Vib. Shock*, vol. 34, no. 12, pp. 35–41, 2015.

[12] M. Zhao and J. C. Ji, "Nonlinear torsional vibrations of a wind turbine gearbox," *Appl. Math. Model.*, vol. 39, no. 16, pp. 4928–4950, Aug. 2015.

[13] L. Shuang, Z. Shuang-Shuang, and S. Bao-Ping, "Bifurcation and chaos analysis of a nonlinear electromechanical coupling relative rotation system," *Chin. Phys. B*, vol. 23, no. 9, pp. 271–277, 2014.
[14] S. Liu, H. Ai, B. Sun, S. Li, and Z. Meng, "Bifurcation and chaos of electromechanical coupling main drive system with strongly nonlinear characteristic in mill," *Chaos, Solitons Fractals*, vol. 98, pp. 101–108, May 2017.
[15] W. Bai, D. Qin, Y. Wang, and T. C. Lim, "Dynamic characteristics of motor-gear system under load saltations and voltage transients," *Mech. Syst. Signal Process.*, vol. 100, pp. 1–16, Feb. 2018.
[16] P. Pennacchi, "Computational model for calculating the dynamical behaviour of generators caused by unbalanced magnetic pull and experimental validation," *J. Sound Vib.*, vol. 312, nos. 1–2, pp. 332–353, Apr. 2008.
[17] R. K. Gustavsson and J.-O. Aidanpää, "The influence of nonlinear magnetic pull on hydropower generator rotors," *J. Sound Vib.*, vol. 297, nos. 3–5, pp. 551–562, Nov. 2006.
[18] N. L. P. Lundström and J.-O. Aidanpää, "Dynamic consequences of electromagnetic pull due to deviations in generator shape," *J. Sound Vib.*, vol. 301, nos. 1–2, pp. 207–225, Mar. 2007.

DONGHAI HU received the B.S. and Ph.D. degrees in automobile engineering from Jiangsu University (UJS), China, in 2011 and 2016, respectively. He is currently an Associate Professor with the School of Automotive and Traffic Engineering, UJS. His research interests include nonlinear dynamic analysis of vehicles, vehicle control of unmanned vehicles, and intelligent vehicles.

JING WANG received the M.S. degree from Jiangsu University. She is currently a Laboratory Teacher with the School of Automotive and Traffic Engineering, UJS.

LELI HU received the B.S. degree in automobile engineering from the School of Automotive and Traffic Engineering, Jiangsu University (UJS), China, in 2018, where he is currently pursuing the M.S. degree in automobile engineering. His research interest is in the area of nonlinear dynamic analysis of vehicles.

JIAMING ZHOU received the M.S. degree from Northwestern Polytechnical University. He is currently pursuing the Ph.D. degree with the Beijing Institute of Technology.

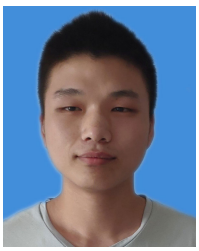

JIE LIU received the B.S. degree in transportation from the School of Automotive Engineering, Shandong Jiaotong University, Sdjtu, China, in 2019, where he is currently pursuing the M.S. degree in transportation engineering. His research interest is in fuel cell systems.